Nanoscale

A Cascade Nanozyme with Antimicrobial Effects against Nontypeable *Haemophilus influenzae*

Journal:	*Nanoscale*
Manuscript ID	NR-COM-08-2022-004306.R1
Article Type:	Communication
Date Submitted by the Author:	15-Dec-2022
Complete List of Authors:	Ma, Xiaojing; Cornell University, Chemical and Biomolecular Engineering Lang, Jiayan; Cornell University, Chemical and Biomolecular Engineering Chen, Pengyu; Cornell University, Chemical and Biomolecular Engineering Tang, Wenjing; Cornell University, Chemical and Biomolecular Engineering Shindler, Simon; Cornell University, Chemical and Biomolecular Engineering Yang, Rong; Cornell University, Chemical and Biomolecular Engineering

COMMUNICATION

A Cascade Nanozyme with Antimicrobial Effects against Nontypeable *Haemophilus influenzae*

Xiaojing Ma,[a] Jiayan Lang,[a] Pengyu Chen,[a] Wenjing Tang,[a] Simon Shindler[a], and Rong Yang*[a]

Received 00th January 20xx,
Accepted 00th January 20xx

DOI: 10.1039/x0xx00000x

Abstract: Otitis media (OM) is a main cause of pediatric antibiotic prescriptions. Nontypeable *Haemophilus influenzae* (NTHi) is a major OM pathogen, which forms biofilm that resists conventional antimicrobials and immune clearance, calling for novel treatments that are effective against NTHi and its biofilm are therefore urgently required. Nanozymes (often inorganic nanoparticles) mimic natural enzymes' catalytic activities to generate strong antimicrobials at the site of infection, and thus represent one of the emerging solutions to the crisis of antimicrobial resistance. They mimic natural enzymes' activities, such as generating strong antimicrobials catalytically at the site of infection, to minimize overexposure. However, that in-situ generation often relies on Reactive Oxygen Species (ROS) as precursors, a prerequisite that limits the broad deployment of nanozymes. To address this challenge, we designed a cascade nanozyme that generates an antiseptic, HOBr, from a ubiquitous non-ROS, i.e., O_2, which successfully eradicates NTHi. The cascade nanozyme simultaneously exhibits glucose oxidase (GOx)-like activity, from gold nanoparticles (AuNPs), and haloperoxidase (HPO)-mimicking activity, from vanadium pentoxide nanowires (V_2O_5 NWs), connected using dopamine (DPA). The cascade nanozyme demonstrated strong antimicrobial efficacy against NTHi and its biofilm, while showing improved biocompatibility compared to the nanozyme of V_2O_5 NWs alone. The cascade nanozyme thus points to a material-oriented infectious disease treatment strategy, where small-molecule antimicrobials are generated in real time at the site of infection for the benefits of autonomous dosing. This strategy potentially mitigates the development of antimicrobial resistance and reduces side effects.

Otitis Media (OM), or middle ear infection, is the most common reason for pediatric antibiotic prescriptions in the US[1], with over 95% of children have had at least one episode of OM by age 5[2,3]. Gram-negative nontypeable *haemophilus influenzae* (NTHi) is one of the major pathogens that invades the auditory bullae opportunistically to cause OM[4–6]. From the largest series of bacteriologic study of pediatric OM (based on middle ear fluid sampling), NTHi is responsible for 16%-61% of all episodes[5] and is identified in up to 60% of persisting episodes[7].

Part of NTHi's resistance is due to its ability to form multicellular biofilm communities, which enables its persistence in the middle ear space[8,9]. Like other biofilm-forming Gram-negative pathogens, NTHi expresses lipopolysaccharides (LPS)[10–13] and type IV pili[14] on the outer membrane during the initial adhesion. In vivo studies have shown that NTHi biofilm could subvert neutrophil extracellular traps that inhibit infection and achieve persistence[8,11,14–16].

Antibiotics, such as ciprofloxacin, amoxicillin with clavulanate, ampicillin, cefotaxime and cefuroxime, are the mainstay of treatment for NTHi-induced OM[17]. Unfortunately, susceptibility of NTHi to ampicillin and cefuroxime has been shown to be below 80% in Poland[18] and 33% in UK (for ampicillin only)[19] and that to cefuroxime is merely 72.1% in China[15]. The frequent and systemic antibiotic exposure associated with NTHi-induced OM has been considered to cause antibiotic resistance, which in turn challenges the treatment efficacy.

Nanomaterials, such as iron nanoparticles, silver nanoparticles, and cerium nanoparticles, with their demonstrated enzyme-like activities (e.g., peroxidase-like activity) have been leveraged as antimicrobials with minimal resistance identified thus far[20–25]. Nanozymes tend to have improved stability and catalytic efficiency in a broader range of temperature and pH with relatively low cost of production compared to natural enzymes[26]. Nevertheless, although nanozymes have shown excellent potential in biomedical and environmental applications[27,28], their use in the treatment of OM and other infectious diseases has been limited .

[a] *Robert F. Smith School of Chemical & Biomolecular Engineering, Cornell University, Ithaca, NY 14853, USA.*
* Corresponding Author, Email: ryang@cornell.edu
Electronic Supplementary Information (ESI) available: [details of any supplementary information available should be included here]. See DOI: 10.1039/x0xx00000x

To bridge that gap, we have previously designed an OM treatment using vanadium pentoxide nanowires (V_2O_5 NWs), which convert a metabolic product (i.e., H_2O_2) of an OM pathogen (i.e., *Streptococcus pneumoniae* (*S. pneumoniae*)) into a potent antiseptic (i.e., HOBr)[29], based on its haloperoxidase (HPO)-mimicking activity[30]. In contrast to the rapid development of resistance to antibiotics such as ciprofloxacin, antiseptics like HOBr are used widely in disinfection without substantial resistance identified to date[31]. Thus, we anticipate the cascade nanozyme to be more effective against resistant strains comparing with small-molecule counterparts. The V_2O_5 NWs mimic vanadium HPOs (V-HPOs) isolated from a marine algae, *Macrocystis Pyrifera*[32], which protect the algae from microbial invaders. While *S. pneumoniae* produces up to 1 mM of H_2O_2 per hour due to its pyruvate oxidase[33], other OM pathogens such as NTHi are not known to produce ROS that is necessary to sustain the HPO reaction, thus rendering V_2O_5 NWs ineffective for treating NTHi.

To treat OM caused by NTHi and its biofilm, we built upon our prior work and designed a cascade nanozyme, composed of V_2O_5 NWs, coated with dopamine (DPA) and surface-decorated with gold nanoparticles (AuNPs). The cascade nanozyme enabled generation of an antiseptic, HOBr, from non-ROS species including Br^-, glucose, and O_2, eradicated NTHi and reduced its biofilm, and mitigated the cytotoxicity commonly observed for V_2O_5 NWs alone. AuNPs were chosen because of their glucose oxidase (GOx)-like activity, which effectively oxidize glucose into gluconic acid and H_2O_2 in the presence of O_2 under a broad range of temperature and pH conditions[27,34]. As such, the cascade nanozyme is designed to sustain the generation of HOBr without the need for *S. pneumoniae*. Below, we first individually characterize the GOx-like activity of AuNPs and the HPO-like catalytic activity of V_2O_5 NWs, and then demonstrate the design and characterization of the cascade enzyme.

To characterize the GOx-like activity of AuNPs, we first measured the rate of H_2O_2 generation as a function glucose concentration (in the range of 0-500 mM) in the presence of 50 μM AuNPs (Fig. 1B). Theoretically, the initial rate of H_2O_2 generation (V_0) follows the Michaelis-Menten equation[35] (eq.1).

$$v_0 = V_{max}\frac{[S]}{K_m + [S]} = k_{cat}[E]_0\frac{[S]}{K_m + [S]} \quad (1)$$

Where [S] is the concentration of substrates such as glucose and O_2 and [E] is the concentration of AuNPs. The Michaelis-Menten constant (K_m) indicates the substrate concentration at which the reaction rate is ½ V_{max} (an indication of binding affinity of a substrate to AuNPs). The values of K_m and maximum reaction rate (V_{max}) were calculated from experimental data using the Lineweaver-Burk linearization (eq. 2).

$$\frac{1}{v_0} = \frac{K_m}{V_{max}} \times \frac{1}{[S]} + \frac{1}{V_{max}} \quad (2)$$

The V_{max} and K_m values were calculated as 1.48 × 10^{-7} M/s and 1.75 × 10^{-5} M respectively. The rate of H_2O_2 production increased as the concentration of glucose increased until the concentration reached 62.5 mM (as shown in Fig. 1B), which was used in subsequent experiments.

In addition, we measured the rate dependence on the concentration of AuNPs (in range of 0-100 μM) in the presence of 62.5 mM glucose. The results indicated that about 2000 μM, 12 μM, 8 μM, and 2.5 μM of H_2O_2 was produced by 100 μM, 3 μM, 2μM, and 1μM of AuNPs respectively over the course of one hour (Fig. S1). We observed that unmodified AuNPs demonstrated a strong tendency to aggregate in solution (Fig. S2), which has been reported previously[27,34], thus calling for stabilization measures.

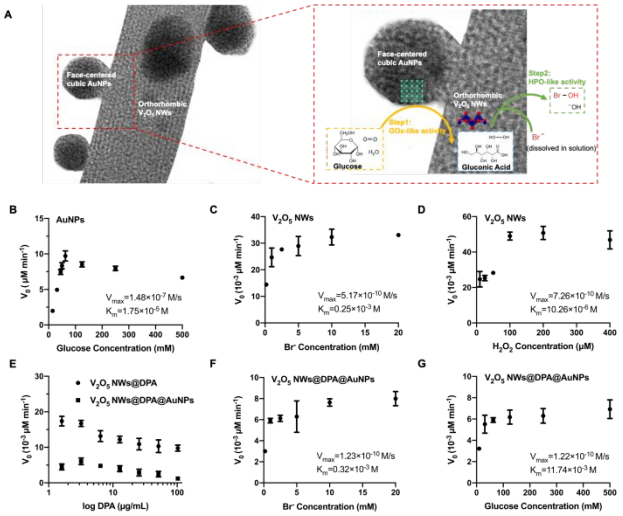

Fig.1. Scheme of V_2O_5 NWs @DPA@AuNPs cascade nanozyme and catalytic activities of AuNPs, V_2O_5, V_2O_5 NWs@DPA, and V_2O_5 NWs @DPA@AuNPs. **(A)** Scheme of catalytic activities of the cascade nanozyme; plotted by adapting TEM images of V_2O_5 NWs@DPA@AuNPs cascade nanozyme in Fig. 4A. **(B)** The initial rate (V_0) of H_2O_2 generation as a function of glucose concentration (in range 0-500mM), collected with 50 μM AuNPs and bubbling air, showed glucose oxidase (GOx)-like activity of AuNPs. **(C)** V_0 of the V_2O_5 NWs as a function of Br^- concentration, collected at the V_2O_5 concentration of 0.02 mg/ml , MCD concentration of 50 μM, and H_2O_2 concentration of 10 μM. **(D)** V_0 of the V_2O_5 NWs as a function of H_2O_2 concentration, collected at the V_2O_5 concentration of 0.02 mg/ml, MCD concentration of 50 μM, and Br^- concentration of 1 mM. **(E)** Dependence of V_0 of the V_2O_5 NWs@DPA (solid circles) and of the V_2O_5 NWs@DPA@AuNPs (solid squares) on DPA concentration, collected at the V_2O_5 concentration of 0.02 mg/ml, MCD concentration of 50 μM, Br^- concentration of 1 mM, and H_2O_2 concentration of 10 μM (for NWs@DPA) or glucose concentration of 62.5 mM (NWs@DPA@AuNPs). **(F)** V_0 of the V_2O_5 NWs as a function of Br^- concentration, collected at the V_2O_5 NWs @DPA@AuNPs concentration of 0.02 mg/ml (in terms of the weight concentration of V_2O_5 NWs), MCD concentration of 50 μM, and glucose concentration of 62.5 mM. **(G)** V_0 of the V_2O_5 NWs as a function of glucose concentration, collected at the V_2O_5 NWs @DPA@AuNPs concentration of 0.02 mg/ml (in terms of the weight concentration of V_2O_5 NWs), the MCD concentration of 50 μM, and the Br^- concentration of 1 mM. Data are

The V_2O_5 NWs were synthesized using a hydrothermal method based on previous reports[30,36]. Transmission electron microscopy (TEM) illustrated the geometry of V_2O_5 NWs, with an average length of 505.6 ± 178.1 nm and an average width of 37.7 ± 12.1 nm (Fig. S3). The atomic percentage of 27.7% Oxygen (O) and 68.1% Vanadium (V) was calculated using scanning transmission electron microscopy with energy dispersive X-ray spectroscopy (STEM-EDX) (Fig. S4A), consistent with previous reports[30,36].

The HPO-mimicking activities of V_2O_5 NWs were quantified using a monochlorodimedone (MCD) assay as described previously[37]. Briefly, the HPO activities lead to bromination of MCD (with absorbance at 290 nm), which creates dihalodimedone with no absorbance at 290 nm (Fig. S5). Thus, the HPO activities could be quantified by monitoring the absorbance at 290 nm. The initial rate (V_0) also follows the

Michaelis-Menten equation[35] (eq.1) as stated above. In this case, [S] is the concentration of Br^- or H_2O_2 and [E] is the concentration of V_2O_5 NWs. To quantify K_m and V_{max}, we individually varied the concentration of substrates while keeping constant concentration of MCD and V_2O_5 NWs at 50 μM and 0.02 mg/mL, respectively (Fig.1C&D). The values of K_m and V_{max} were calculated (using eq. 2) as 0.25×10^{-3} M and 10.26×10^{-6} M for Br^- and H_2O_2 respectively (for K_m) and 5.17×10^{-10} M/s and 7.26×10^{-10} M/s for Br^- and H_2O_2 respectively (for V_{max}), which are comparable to the values reported in previous work[30]. The K_m values indicate relatively high affinity of H_2O_2 to V_2O_5 NWs.

Antimicrobial activity of V_2O_5 NWs was verified using NTHi. The optical density at 600 nm (OD600) of NTHi was recorded over 7 hours (Fig. 2A). The groups of NTHi only, NTHi treated with 1mM Br^- and 20 μM H_2O_2 (to test the influence of Br^- and H_2O_2 alone), NTHi treated with 0.04 mg/mL V_2O_5 NWs (to test the antimicrobial effect of V_2O_5 NWs alone), NTHi treated with 0.04 mg/mL V_2O_5 NWs and 1 mM of Br^-, and NTHi treated with 0.04 mg/mL V_2O_5 NWs, 1 mM Br^-, and 20 μM H_2O_2 were compared (Fig. 2A). The results showed that at least a subpopulation of NTHi remained after the treatment of Br^- and H_2O_2, or V_2O_5 NWs alone, or V_2O_5 NWs with Br^-; whereas NTHi was completely eradicated after the treatment of Br^-, H_2O_2, and V_2O_5 NWs. This result confirmed that NTHi could not generate H_2O_2 although V_2O_5 NWs were effective, as when H_2O_2 was introduced exogenously the treatment system was strongly antimicrobial. It is noteworthy that dead cells and cell debris could cause false OD600 reading. We thus took an aliquot (100 μL) of the NTHi culture, treated with Br^-, H_2O_2, and V_2O_5 NWs (at the end of the 7-hour incubation), and plated it onto a chocolate agar to confirm the complete loss of viability of NTHi. No growth was observed on the agars, indicating that the minimum inhibitory concentration (MIC) of V_2O_5 NWs (with Br^- and H_2O_2) was comparable to the minimum bactericidal concentration (MBC).

To enable the cascade catalytic reactions, we first physically mixed the V_2O_5 NWs and AuNPs and tested the antimicrobial effects using NTHi. No antimicrobial effects were detected when adding glucose, Br^-, and O_2, whereas bacterial growth was inhibited when adding H_2O_2 and Br^- (Fig. S6A). These results implied that V_2O_5 NWs were catalytic, but the physically mixing approach failed at producing cascade actions.

Based on the robust reactivity of V_2O_5 NWs, we subsequently synthesized AuNPs *in situ*, i.e., in the presence of V_2O_5 NWs, in hope of achieving a homogeneous mixture of the two nanomaterials and shorten the delivery distance needed for H_2O_2 (i.e., the distance between generation on AuNPs to consumption on V_2O_5 NWs). Briefly, a solution of V_2O_5 NWs was mixed with $HAuCl_4$ and subsequently $NaBH_4$ to generate AuNPs. No antimicrobial effects were detected of the V_2O_5 NWs decorated with *in-situ* grown AuNPs when tested with NTHi culture (in glucose, Br^-, and O_2 or in H_2O_2 and Br^-) (Fig. S6B). The results implied that V_2O_5 NWs lost their catalytic activity during the *in-situ* synthesis of AuNPs. That deactivation of the catalytic activity of V_2O_5 NWs was likely due to the strongly reducing agent, $NaBH_4$, that was used to synthesize AuNPs[38].

Based on the results from physically mixing V_2O_5 NWs and AuNPs and those from synthesizing AuNPs in the presence of V_2O_5 NWs, we proposed that a protection layer is required to retain the catalytic activity of V_2O_5 NWs during AuNPs synthesis, which should also improve the adhesion of AuNPs onto the surface of V_2O_5 NWs to shorten the diffusion length required for H_2O_2. As such, we designed our cascade nanozyme with a dopamine (DPA) coating on V_2O_5 NWs and subsequent surface decoration via AuNPs, i.e., V_2O_5 NWs@DPA@AuNPs. In this system, DPA serves as a protection layer for V_2O_5 NWs to avoid their deactivation (by the strong reducing agent $NaBH_4$) and as an adhesive to concentrate as-synthesized AuNPs onto the surface of V_2O_5 NWs.

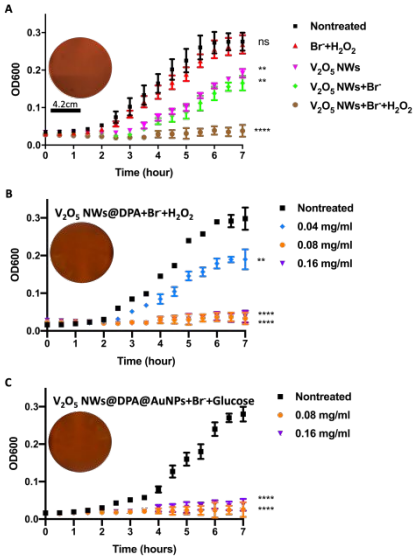

Fig.2. Antibacterial effects of the V_2O_5 NWs, V_2O_5 NWs@DPA and V_2O_5 NWs@DPA@AuNPs cascade nanozyme. Bacterial growth curves (OD600) of NTHi were monitored for 7 hours during the incubation with **(A)** 0.04 mg/mL V_2O_5 NWs, 1 mM Br^-, and 20μM H_2O_2, **(B)** 0.04 mg/mL, 0.08 mg/mL, or 0.16 mg/mL (in terms of the weight concentration of V_2O_5 NWs) V_2O_5 NWs@DPA, 1mM Br^-, and 20 μM H_2O_2, **(C)** 0.08 mg/mL or 0.16 mg/mL V_2O_5 NWs@DPA@AuNPs, 1 mM Br^-, and 62.5 mM glucose with bubbling air. Images of the chocolate agar plates were obtained by plating the NTHi cultures with 0.04 mg/ml V_2O_5 NWs+H_2O_2+Br^-, or 0.08 mg/ml V_2O_5 NWs@DPA+Br^-+H_2O_2, or 0.08 mg/ml V_2O_5 NWs@DPA@AuNPs+Br^-+glucose at the end of the 7-hour incubation. Data are mean ± SD. n = 4. ns, not statistically significant, $^{**}p<0.01$, and $^{****}p<0.0001$; all comparisons were made with respect to the "Nontreated" group. Scale bar is 4.2cm.

Notably, this cascade nanozyme generates a strongly oxidizing antiseptic (i.e., HOBr) from non-Reactive Oxygen Species (non-ROS) (i.e., glucose, O_2 and Br^-), which is distinct from previously reported nanozymes. That feature in turn leads to complete eradication of planktonic NTHi and inhibition of its biofilm while mitigating the observed cytotoxicity of V_2O_5 NWs alone. To the best of our knowledge, this is the first time that a cascade nanozyme system has been used in treating OM[39].

DPA was chosen because it can self-polymerize onto the surface of V_2O_5 NWs (forming V_2O_5 NWs@DPA at pH 8.0) (Fig. 1A). To deposit a sufficient amount of DPA on the surface of V_2O_5 NWs, the weight ratio of V_2O_5 NWs to DPA was systematically varied during the DPA coating step by adding DPA to a constant concentration of V_2O_5 NWs, in two-fold serial

diluted amounts (i.e., 1 mg of V_2O_5 NWs with 1.6, 3.2, 6.4, 12.8, 25.6, 51.2, and 102.4 µg of DPA respectively). The dependence of V_0 of the bromination reaction on DPA amount was studied using V_2O_5 NWs@DPA at the V_2O_5 NWs concentration of 0.02 mg/mL, MCD concentration of 50 µM, H_2O_2 concentration of 10µM, and Br^- concentration of 1mM (Fig. 1E). The results indicated that V_0 decreases with increasing amount of DPA coating, implying potential coverage of catalytic sites on V_2O_5 NWs by DPA. V_2O_5 NWs@DPA obtained using 1.6, 3.2, and 6.4 µg DPA in 1 mg V_2O_5 NWs reduced the V_0 (of V_2O_5 NWs alone) by 39.7%, 32.2%, and 43.3% respectively (Fig. 1E).

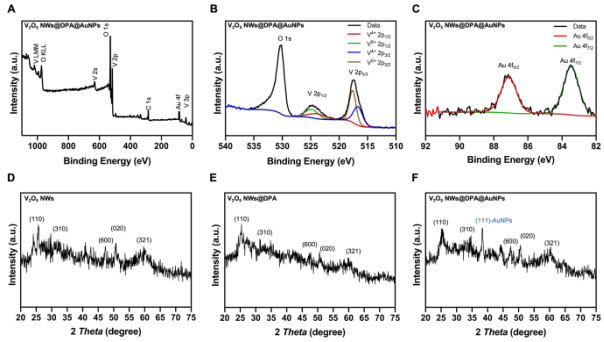

Fig.3. Elemental composition of V_2O_5 NWs and V_2O_5 NWs@DPA@AuNPs cascade nanozyme. (A) XPS survey scan of the V_2O_5 NWs@DPA@AuNPs cascade nanozyme. **(B)** High-resolution XPS spectra of O(1s), V($2p_{1/2}$), and V($2p_{3/2}$) in V_2O_5 NWs@DPA@AuNPs cascade nanozyme. **(C)** High-resolution XPS spectra of the Au($4f_{5/2}$) and Au($4f_{7/2}$) in V_2O_5 NWs@DPA@AuNPs cascade nanozyme. XRD diffractograms of **(D)** V_2O_5 NWs, **(E)** V_2O_5 NWs@DPA, and **(F)** V_2O_5 NWs@AuNPs cascade nanozyme

The catalytic activity of V_2O_5 NWs@DPA (synthesized using 3.2 µg DPA per 1 mg V_2O_5 NWs), which showed the least reduction of V_0, was then tested using NTHi. For doing that, 0.04, 0.08, and 0.16 mg/mL V_2O_5 NWs@DPA with 1mM Br^- and 20 µM H_2O_2 were incubated with NTHi for 7 hours to show the effectiveness of V_2O_5 NWs@DPA at converting H_2O_2 and Br^- into HOBr and then eradicating NTHi (Fig. 2B). The OD600 results showed that 0.08 mg/mL V_2O_5 NWs@DPA with 20 µM H_2O_2 and 1 mM Br^- could eradicate NTHi completely, which was also confirmed by plating 100 µL culture onto chocolate agar. The results implied that the MIC and MBC of V_2O_5 NWs@DPA were similar. The MIC of V_2O_5 NWs@DPA was two times higher than that of V_2O_5 NWs alone, which was likely a result of DPA covering the active sites on the surface of V_2O_5 NWs. The antimicrobial efficacy of a physical mixture of V_2O_5 NWs@DPA and AuNPs was also assessed using NTHi (Fig. S6C). Unsurprisingly, no detectable antimicrobial activity was captured for the physical mixture (in the presence of glucose, Br^-, and O_2), corroborating the importance of placing the two catalytic steps, enabled by AuNPs and V_2O_5 NWs, respectively, right next to each other to enable the cascade activity. Then, the V_2O_5 NWs@DPA was subsequently decorated with AuNPs as illustrated in Fig. 1A. Briefly, DPA coating was applied onto the surface of V_2O_5 NWs (V_2O_5 NWs@DPA) at pH 8.0 and AuNPs were synthesized *in situ*. The DPA layer provides protection for V_2O_5 NWs and heterogeneous nucleation sites for the as-synthesized AuNPs[38], promoting their adhesion and preventing aggregation[27,34]. The scheme of the synthesis steps to obtain the cascade nanozyme in supporting information as Fig. S7. We subsequently characterized the cascade nanozyme, V_2O_5 NWs@DPA@AuNPs, for its elemental composition, bonding environmental, geometry, and crystallography as described below.

Elemental composition of V_2O_5 NWs@DPA@AuNPs was characterized using X-ray photoelectron spectroscopy (XPS) (Fig. 3A-C). The atomic percentage of O, V, N, and Au is about 76.78%, 17.13%, 4.66%, and 1.43% respectively. To confirm that the correct bonding environments were obtained for V_2O_5

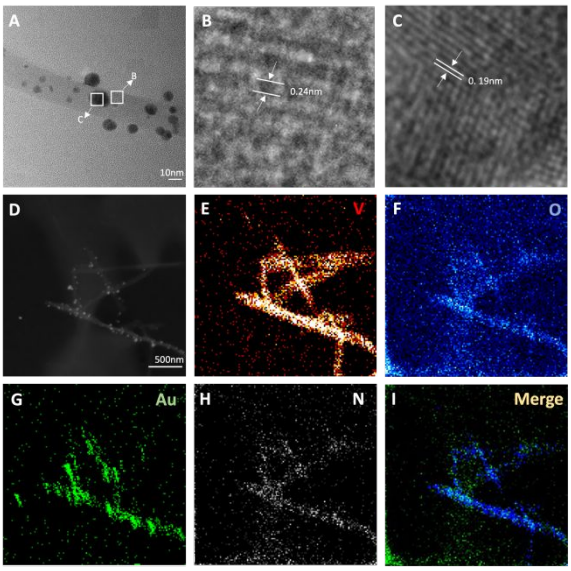

Fig.4. TEM analysis of V_2O_5 NWs@DPA@AuNPs cascade nanozyme. (A) TEM image of V_2O_5 NWs@DPA@AuNPs cascade nanozyme, showing the overall assembly of AuNPs on the surface of V_2O_5 NWs. **(B)** HRTEM of the V_2O_5 lattice structure and lattice size in V_2O_5 NWs@DPA@AuNPs (zooming into the box in panel A that is labelled "B"). **(C)** HRTEM of the lattice structure and lattice size of the AuNPs from V_2O_5@DPA@AuNPs (zooming into the box in panel A that is labelled "C"). **(D)** Dark-field STEM image, showing the dimensions of the V_2O_5 NWs and the distribution of AuNPs. **(E-I)** EDX elemental mapping of V, O, Au, N, and their merged image that corresponds to panel D.

NWs and AuNPs, XPS high-resolution scans on V (2p), O(1s), and Au (4f) were collected (Fig. 3). The peaks at 517.2 eV, 524.9 eV, and 530.1 eV (±0.1 eV) correspond to the spin-orbit split of V (2p3/2), V (2p1/2), and O (1s) respectively (Fig. 3B). The V (2p) peaks demonstrated an area ratio of 2:1 and a separation of 7.7 eV, comparable to those reported in previous literature[40]. The high resolution XPS spectra was further deconvoluted (Fig. 3B), confirming that V(V) was the dominating oxidation state despite minor presence of V(IV), likely due to incomplete oxidation, which gave rise to VO_2[40,41]. The O (1s) spectrum contained the lattice oxygen at 535 eV[42], the -OH groups on the lattice surface at 531.5 eV[40,43], and the surface-absorbed water at 533 eV[40]. The Au (4f) spectrum exhibited two spin-orbit, Au (4f7/2) and Au (4f5/2), separated by 3.7 eV (Fig. 3C), as shown in the peak deconvolution, representative of metallic Au^0 species[44]. The XPS results thus confirmed the correct elemental composition and oxidation states of the constituents of the cascade nanozyme system.

X-ray powder diffraction (XRD) patterns were then collected and analysed (Fig. 3D-F). The diffractogram of the V_2O_5 NWs and V_2O_5 NWs@DPA exhibited the characteristic peaks corresponding to the (110), (310), (600), (020), and (321) planes of an orthorhombic structure of V_2O_5 NWs (Fig. 3D-E), consistent with previous reports[45,46]. The set of peaks was also identified in the diffractogram of V_2O_5 NWs@DPA@AuNPs, (Fig. 3F) indicating excellent retainment of the crystalline structures during the synthesis and modification procedure. An additional peak emerged in the diffractogram of V_2O_5 NWs@DPA@AuNPs, at 38 degrees, which we attributed to the (111) plane of the AuNPs. That attribution is supported by the XRD on AuNPs alone (Fig. S8), which exhibited peaks at (111), (200), (220), and (311) that collectively point to a face-centered cubic (fcc) structure of Au atoms[47,48].

The TEM images of V_2O_5 NWs@DPA@AuNPs clearly exhibited spherical AuNPs with an average diameter of 6.2 ± 1.7 nm, which were randomly distributed on the surface of V_2O_5 NWs@DPA (Fig. 4A). High-resolution TEM (HRTEM) images evidenced V_2O_5 NWs, that of N represented DPA, and Au indicated the presence of AuNPs (Fig. 4D-I, Fig. S4B).

The DPA coating and surface-attached AuNPs can reduce the catalytic activity of V_2O_5 NWs via physical blockage of the active sites on the surface of V_2O_5 NWs. To explore that trade off, the ratio of DPA to V_2O_5 NWs and that of AuNPs to V_2O_5 NWs were varied systematically and the resulting cascade enzymatic activity was quantified, as discussed below. The catalytic activities of V_2O_5 NWs@DPA@AuNPs cascade nanozyme were characterized by the MCD method and calculated using eq.1, where [S] is the concentration of Br^- or glucose, or H_2O_2, and [E] is the concentration of the cascade nanozyme (indicated by the weight concentration of V_2O_5 NWs).

The V_2O_5 NWs@DPA synthesized using 3.2 µg DPA per 1 mg V_2O_5 NWs was used in this characterization due to its successful retainment of V_2O_5 reactivity (as shown by its V_0 in Fig. 1E). AuNPs (at 2 µM) were used to produce the V_2O_5 NWs@DPA@AuNPs composite, which was subsequently used in the MCD method. The MCD results showed that the V_2O_5

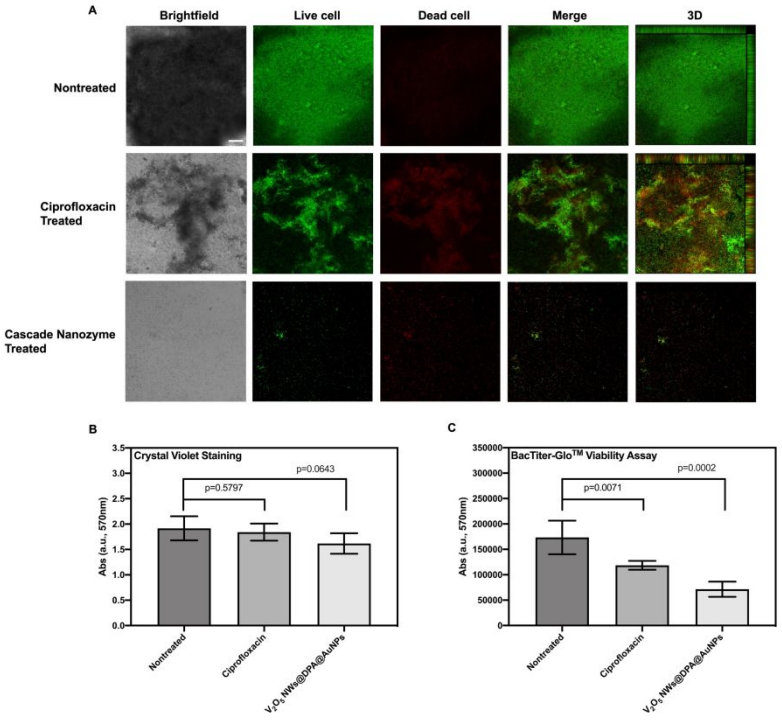

Fig.5. Antibiofilm effects of V_2O_5 NWs@DPA@AuNPs cascade nanozyme and comparison with a common small-molecule antibiotic, ciprofloxacin. NTHi biofilm was treated with the antimicrobials at their respective MICs for 24 hours after three days of incubation. **(A)** Confocal images of the nontreated NTHi biofilm and NTHi biofilm treated with V_2O_5 NWs@DPA@AuNPs cascade nanozyme and ciprofloxacin, respectively, and stained with the BacTiter-Glo™ Microbial Cell Viability Assay. Scale bar is 50 µm. **(B)** Quantification of the crystal violet staining results of nontreated NTHi biofilm and NTHi biofilm treated with the cascade nanozyme and ciprofloxacin respectively. **(C)** Quantification of the BacTiter-Glo™ Microbial Cell Viability Assay of nontreated NTHi biofilm and biofilm treated with the cascade and ciprofloxacin respectively. Data are mean ± SD. n=5.

demonstrated the (020) lattice plane in the orthorhombic phase of the V_2O_5 NWs with a d-spacing of ~0.24 nm (Fig. 4B). The (200) lattice plane in the fcc structure of AuNPs was also identified in the HRTEM (Fig. 4C), with the d-spacing of ~0.19 nm. The STEM-EDX further showed the elemental mapping of V_2O_5 NWs@DPA@AuNPs, where the presence of V and O NWs@DPA@AuNPs exhibited a reduced V_0 by merely 2.27% compared to V_2O_5 NWs@DPA. The V_0 value was reduced by 63.7% compared to V_2O_5 NWs@DPA when reacted with glucose, O_2, and Br^- (Fig. S9). The K_m of V_2O_5 NWs@DPA@AuNPs cascade nanozyme was calculated as 0.32 × 10^{-3} M and 11.74 × 10^{-3} M for Br^- and glucose respectively, and the V_{max} as 1.23 × 10^{-10} M/s and 1.22 × 10^{-10} M/s for Br-

and glucose respectively (Fig. 1F&G), indicating higher affinity of Br^- to the cascade nanozyme compared to V_2O_5 NWs@DPA@AuNPs cascade nanozyme. The details about the cascade nanozymes synthesis can be found in SI. We found that the V_2O_5 NWs@DPA@AuNPs synthesized using 3.2 μg DPA and 2 μM AuNPs per 1 mg V_2O_5 NWs showed the highest catalytic activity for the cascade nanozymes which would use for the following experiments.

Next, 0.08 and 0.16 mg/mL V_2O_5 NWs@DPA@AuNPs (i.e., in terms of weight concentration of V_2O_5 NWs) with 1 mM Br^-, 62.5 mM glucose, and bubbling air were incubated with NTHi for 7 hours. The results showed that 0.08 mg/mL V_2O_5 NWs@DPA@AuNPs inhibited growth of NTHi (Fig. 2C). 100μL of the NTHi culture was plated onto chocolate agar to confirm the results of OD600, confirming complete eradication of NTHi under these conditions. We believe that the antimicrobial efficacy was not due to cytotoxicity of the cascade nanozyme (despite its higher MIC than V_2O_5 NWs). That conclusion was made based on the results from (i) a physical mixture of V_2O_5 NWs and AuNPs, and (ii) a physical mixture of V_2O_5 NWs@DPA and AuNPs, which provided an assessment of the cytotoxicity. Here, "cytotoxicity" is defined as the non-specific damages to the bacteria cells that were not caused by the antiseptics generated via the cascade enzymatic activities. The two aforementioned control groups demonstrated minimal cascade enzymatic activities in vitro (Fig. S6), and thus any antimicrobial effects demonstrated by these control groups should be attributed to cytotoxicity. As shown in Fig. 2 and Fig. S6, OD600 of NTHi was reduced by 9.54% when incubated with a physical mixture of the V_2O_5 NWs and AuNPs (in the presence of glucose, Br^-, and O_2); OD600 was reduced by 8.73% when incubated with a physical mixture of the V_2O_5 NWs@DPA and AuNPs (in the presence of glucose, Br^-, and O_2). As such, complete eradication of NTHi is only achieved via the cascade enzymatic activities although mild cytotoxicity may have contributed to the overall antimicrobial effects. The MIC of V_2O_5 NWs@DPA@AuNPs was twice that of V_2O_5 NWs alone, but similar to the MIC of V_2O_5 NWs@DPA, indicating good compatibility of AuNPs with V_2O_5 NWs and implying that the decoration by AuNPs did not further block the active sites on V_2O_5 NWs. The excellent antimicrobial efficacy against planktonic NTHi points to the potential of the cascade nanozyme as a future therapeutic to mitigate the systemic antibiotic exposure and resistance development during the treatment of an extremely prevalent pediatric disease.

We are also interested in the effects of the cascade nanozyme on bacterial biofilms, as the nanorod shape could lead to improved penetration of the biofilm and thus improved biofilm mitigation compared to existing antibiotics like ciprofloxacin. The NTHi biofilm growth curve over 5 days was obtained via staining of the biofilm with crystal violet and quantification by dissolving absorbed crystal violet in 30% (v/v) acetic acid to measure absorbance at 570 nm (Fig. S11). NTHi formed relatively stable biofilms starting at day 3, upon the confirmation of which the V_2O_5 NWs@DPA@AuNPs cascade nanozyme was added to the liquid culture to its MIC (i.e., 0.08 mg/mL) for a 24-hour incubation. The treated biofilms were then quantified by crystal violet staining for total cell (both dead and live) and BacTiter-Glo™ Microbial Cell Viability Assay for live cells (based on the quantitation of ATP). Using crystal violet staining, treated biofilms were quantified to have a total cell count reduction of 15.61%, compared to the nontreated group (Fig. 5B), whereas BacTiter-Glo™ revealed a reduction of live cell count of 58.80% compared to the nontreated group (Fig. 5C). The MIC of a commercial antibiotic, ciprofloxacin (0.4 μg/mL for planktonic NTHi) (Fig. S12) was used to treat NTHi biofilms as a point of comparison. Similar to the treatment using the cascade nanozyme, the biofilms were grown for 3 days and treated with ciprofloxacin for 24 hours. Crystal violet staining and BacTiter-Glo™ revealed a 3.92% reduction in total cell counts (Fig. 5B) and a 31.66% reduction in the count of live cells in the treated biofilm (Fig. 5C). When treated with 0.08 mg/ml V_2O_5 NWs (alone) for 24 hours, the NTHi biofilm demonstrated a reduction of 10.02% in the total cell count (via crystal violet staining), and a reduction of 23.07% in the count of live cells (via the BacTiter-Glo™ assay) (Fig. S15). These results combined illustrated that, when tested at their respective MICs, the cascade nanozyme led to much greater mitigation of NTHi biofilms than the small molecule antibiotic, ciprofloxacin, eliminating a majority of the live cells in the biofilm. By comparing the performance of the V_2O_5 NWs (alone) with the cascade nanozyme, we conclude that the nano-dimensions of the V_2O_5 NWs enhanced their penetration into the biofilm, whereas the catalytic activities of the cascade nanozyme was responsible for the antimicrobial effect against NTHi biofilm.

To address the issue of incomparability of different drug types, their respective MIC's were used to "calibrate" the concentrations used in the anti-biofilm tests. Note that no direct comparison was made between the MIC's of ciprofloxacin and the nanozymes. Instead, their MIC values were used to benchmark the sensitivity of NTHi biofilms against the sensitivity of NTHi planktonic cells when treated using these two types of drugs. Biofilms are known to be antibiotic-resistant, i.e., they are insensitive to antibiotics at concentrations that planktonic cells are. Therefore, if a therapeutic is efficacious against biofilm at its MIC for planktonic bacteria, the therapeutic would be considered anti-biofilm; whereas if a therapeutic is inefficacious against biofilm at its MIC for planktonic bacteria, it would be resisted by biofilm, which is the case for common antibiotics[49,50]. Through this "calibration" using their respective

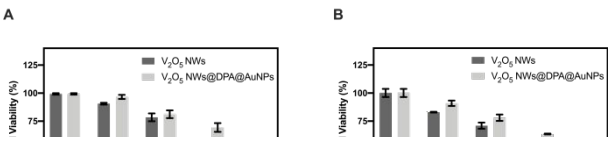

Fig.6. Biocompatibility assessment in vitro. (A) hFBs cells were incubated with V_2O_5 NWs and V_2O_5 NWs @DPA@AuNPs in the concentration range of 0 to 0.08 mg/ml (in terms of weight concentration of V_2O_5 NWs), 1 mM Br^-, and 20 μM H_2O_2 (V_2O_5 NWs) or 62.5 mM glucose (V_2O_5 NWs @DPA@AuNPs) with bubbling air for 24 hours **(B)** hFBs cells were incubated with V_2O_5 NWs and V_2O_5 NWs @DPA@AuNPs in the concentration range of 0 to 0.08 mg/ml (in terms of weight concentration of V_2O_5 NWs), 1 mM Br^-, and 20 μM H_2O_2 (V_2O_5 NWs) or 62.5 mM glucose (V_2O_5 NWs @DPA@AuNPs) with bubbling air for 48 hours. Data are mean ± SD. n = 4.

MIC's, different classes of therapeutics can be compared for their anti-biofilm efficacy.

This result was confirmed using confocal fluorescence microscopy (Fig. 5A). The NTHi biofilm treated with ciprofloxacin for 24 hours maintained the dense morphology and original thickness, confirming the resistance of NTHi biofilms to small-molecule antibiotics. In contrast, the biofilm treated with the cascade nanozyme was broken into small pieces (Fig. S13), pointing to the ability of the cascade nanozyme to penetrate the biofilm and/or deliver the generated HOBr into the internal structures of the biofilm. Note that the MIC of the cascade nanozyme is much greater than that of ciprofloxacin, indicating higher sensitivity of planktonic NTHi towards ciprofloxacin than that to the cascade nanozyme. Nevertheless, we evaluated their efficacy against biofilms at their respective MIC (instead of using the same absolute concentration), because it is our intention to assess their ability to mitigate biofilms without the interference from their absolute antimicrobial efficacy. It is thus an important focus of our future work to improve the efficacy of the cascade nanozymes against planktonic NTHi, which we anticipate would yield much greater efficacy and hopefully complete eradication of NTHi biofilms.

The in vivo efficacy of the cascade nanozyme was assessed in a well-established NTHi-induced OM model using chinchillas, as detailed below. The timeline for infection establishment, treatment, and sample collection for the in vivo assessment is shown in Fig. S16. In brief, the auditory bullae were dry and sterile under healthy conditions, into which NTHi was directly inoculated through the dorsal aspect of the bullae on day -3 (whereas the time of treatment administration was used as day 0). Once successful infection was confirmed, the middle ear fluid (MEF) of the treated and nontreated animals was collected for serial dilution and NTHi culture to quantify the colony-forming unit (CFU) in the middle ear, for which a value greater than 10^4 CFU was used as an indication of successful establishment of infection[51]. Once infection was established, on Day 0, 200μL of a formulation containing 0.16 mg/mL cascade nanozyme, 1 mM Br^-, and 62.5 mM glucose was injected through the auditory bullae. MEF was extracted from the dorsal aspect of the auditory bullae on day 1, 3, and 7 to monitor NTHi growth in the middle ear. The number of CFU in the MEF of infected and treated animals was reduced by about 100 times, where as a reduction of 1000-fold is often considered complete cure in the OM literature[52,53]. We attributed that insufficient efficacy to the lack of access to O_2 in the closed environment of an auditory bulla.

Finally, we assessed the cytotoxicity of V_2O_5 NWs and V_2O_5 NWs@DPA@AuNPs cascade nanozyme using human fibroblast cells (hFBs) and the Cell Counting Kit 8 (CCK-8 kit). The concentration range of 0 to 0.08 mg/ml (in terms of weight concentration of V_2O_5 NWs) was used for V_2O_5 NWs and V_2O_5 NWs@DPA@AuNPs, along with 1 mM Br^-, and 20 μM H_2O_2 (for V_2O_5 NWs) or 62.5 mM glucose and bubbling air (for V_2O_5 NWs@DPA@AuNPs). The hFBs cells were incubated with the formulations for 24 hours and 48 hours prior to CCK-8 evaluation (Fig. 6). At 0.01 mg/mL, neither formulation led to cytotoxicity. Mild cytotoxicity was observed at 0.04 mg/mL, with the 24-hour cell viability of 54.81 ± 0.62% and 69.39 ± 3.92% and 48-hour cell viability of 47.46 ± 0.30% and 63.51 ± 0.31%for V_2O_5 NWs and V_2O_5 NWs@DPA@AuNPs respectively. Severe cytotoxicity was observed for 0.08 mg/mL V_2O_5 NWs, with 24- and 48-hour cell viability of 29.91 ± 4.10% and 24.68 ± 1.41%, whereas that for 0.08 mg/mL V_2O_5 NWs@DPA@AuNPs remained mild, with 24- and 48-hour viability of 55.47 ± 3.60% and 47.34 ± 0.78%. The lower cytotoxicity demonstrated by the cascade nanozyme, compared to that of V_2O_5 NWs alone, was likely a result of the DPA coating and AuNPs coverage, which effectively prevented cell damage.

Discussions and Conclusions

We have successfully synthesized a cascade nanozyme, V_2O_5 NWs@DPA@AuNPs, which generates an effective antiseptic, i.e., HOBr, from non-ROS reactants including glucose, Br^-, and O_2. The cascade nanozyme was demonstrated effective at eradicating planktonic NTHi, when added to the bacteria culture to concentrations as low as 0.08 mg/mL.

That antimicrobial efficacy stems from the dual catalytic activities, which combine (i) GOx-like activity of AuNPs that converts glucose and O_2 to generate H_2O_2 and (ii) HPO-like activity of V_2O_5 NWs that converts H_2O_2 to an antiseptic, HOBr. The cascade nanozyme was enabled by a DPA coating layer on V_2O_5 NWs, which allows the subsequent *in-situ* synthesis of AuNPs that we proved to be key to obtaining the cascade enzymatic activities. In particular, the DPA coating serves three functions: (i) to protect V_2O_5 NWs in the strongly reducing environment that is required for the synthesis of AuNPs, (ii) to promote heterogeneous nucleation of AuNPs on the surface of V_2O_5 NWs [38], and (iii) to protect as-synthesized AuNPs from aggregation. The direct contact between AuNPs and V_2O_5 NWs effectively shortens the delivery distance needed for H_2O_2 (i.e., the distance between generation on AuNPs to consumption on V_2O_5 NWs) and thus made the cascade catalytic reactions a success.

To optimize the catalytic activities, the composition and concentrations of each constituent in the cascade nanozyme, V_2O_5 NWs@DPA@AuNPs, were varied systematically, and the combination of 3.2 μg DPA per 1 mg of V_2O_5 NWs, along with 2 μM AuNPs per 1 mg of V_2O_5 NWs was chosen as the optimum cascade nanozyme. Lower concentrations of DPA or AuNPs do not generate sufficient H_2O_2 and higher concentrations tend to block the active catalytic sites on V_2O_5 NWs. TEM, XPS, and XRD were used to confirm that AuNPs were successfully synthesized and adhered onto the surface of V_2O_5 NWs (in the presence of DPA coatings), and AuNPs and V_2O_5 NWs exhibited the correct valence. We characterized the cascade catalytic reactions and the reaction kinetics of each step in great details and illustrated that the cascade nanozyme generates HOBr from glucose, Br^-, and O_2 with comparable kinetics to naturally occurring HPOs reported previously[30].

MIC of the cascade nanozyme was determined to be 0.08 mg/mL for planktonic NTHi, demonstrating complete eradication at the end of the 7-hour culture, which we further confirmed by plating on chocolate agar. The cascade nanozyme

also demonstrated greater efficacy against NTHi biofilms compared to a common small-molecule antibiotic, ciprofloxacin, when both were applied at their respective MIC. Both the total cell count (indicated by crystal violet staining) and the count of live cells within a biofilm (indicated by the BacTiter-Glo™ Microbial Cell Viability Assay) were used to illustrate the effectiveness of the cascade nanozyme, with over half of the live cells eradicated in a biofilm when treated with the nanozyme. Those results were further confirmed by confocal images, highlighting the unchanged morphology of biofilms upon treatment with ciprofloxacin and the minimal biofilm remaining after the treatment with the cascade nanozyme. Cytotoxicity results, obtained using hFBs, pointed to the reduced toxicity of the cascade nanozyme compared to V_2O_5 NWs alone.

Nanozymes, especially metal oxide nanoparticle-based catalytic systems, have not been broadly used in infectious disease treatment, most likely due to the presumed biocompatibility issues. Inorganic nanomaterials have been reserved for the most severe diseases like cancer due to their demonstrated tissue and systemic toxicity. Metal oxide nanozymes are known to generate harmful free radicals under physiological conditions[54]. Nevertheless, this work leverages that presumed harmful generation of radicals as a mechanism to eradicate infectious pathogens. It is vital that the treatment is delivered locally to the site of infection and not systemically and that their presence remains localized throughout the treatment until the disease is cured and the nanozymes are cleared out of the system. In that sense, OM is a perfect disease model for the deployment of these nanozymes. The auditory bullae function as an enclosed "reactor" for the catalytic generation of antiseptics; upon eradication of OM, the nanozymes can be cleared quickly through the eustachian tube and nasopharynx, which is commonly clogged during infection but cleared up upon successful treatment. Furthermore, recent advances in inorganic nanowires, such as silicon nanowires, and their successful medicinal application can guide the development of metal oxide nanozymes to achieve biocompatibility. Silicon nanowires, pioneered by Timko, Lieber, et. al[55–57], have been shown to be biodegradable and their degradation products highly biocompatible. There have been an increasing number of reports in recent years on application of nanozymes to treat infectious diseases, including our recent work demonstrating the successful treatment of OM caused by *S. pneumoniae* using V_2O_5 NWs, as well as the eradication of a human corona virus using ceria nanoparticles. We believe these early proof-of-principles provide strong evidence for the promise of metal oxide nanozymes as an effective and safe therapeutic for local infections.

To the best of our knowledge, this represents the first cascade nanozyme that has been used for treating OM pathogens. Its efficacy against NTHi biofilm points to a potential solution to the pervasive issue of recurring OM episodes and the frequent and systematic antibiotic exposure associated with those episodes. Our future work will focus on optimizing and reducing the MIC of the cascade nanozyme system or similar systems, which would in turn improve the efficacy against biofilms that are resistant to the treatment using conventional small-molecule antibiotics. In addition, the formulation should be optimized to enhance the availability of oxygen in the closed environment of an auditory bulla. Strategies like replacing the water-based solvent used in the formulation with one that has high oxygen solubility, or including oxygen-loaded particles into the current formulation[58], may yield successful in vivo results. While most other nanozymes reported to date rely on ROS as a precursor for the in-situ synthesis of antiseptics, the cascade nanozyme does not require ROS. The removal of that prerequisite greatly broadens the scope of potential applications for similar catalytic therapeutics. Here we demonstrate one potential deployment in treating OM caused by NTHi, which could not be eradicated using previous nanozymes that rely on ROS. In addition, the cascade nanozyme is effective against biofilms, which is known to be antibiotic-resistant. Benchmarked by their respective MIC for planktonic NTHi, the cascade nanozyme demonstrated stronger efficacy against NTHi biofilm compared to ciprofloxacin. This cascade nanozyme design has the potential to replace conventional antibiotics in the treatment and prophylaxis of OM, reducing the development of drug resistance and side effects associated with the current mainstay treatment.

Author Contributions

XM, JL, and RY conceived the idea and designed the experiments. XM and JL synthesized the cascade nanozyme. XM, PC, WT, and SS conducted the experiments. XM and RY performed the data analysis. RY supervised the study. The manuscript was prepared by XM and RY.

Conflicts of interest

Authors state that there are no conflicts to declare.

Acknowledgements

This work was supported by the Department of Defense, Office of Naval Research (ONR award N00014- 20-1-2418); National Institutes of Health, National Institute on Deafness and Other Communication Disorders (NIHDC016644).

Notes and references

1 C. R. Paul and M. A. Moreno, *JAMA Pediatr.*, 2020, **174**, 308.

2 D. W. Teele, J. O. Klein and B. Rosner, *J. Infect. Dis.*, 1989, **160**, 83–94.

3 A. D. Shaffer, M. D. Ford, S. S. Choi and N. Jabbour, *Cleft Palate-Craniofacial J.*, 2019, **56**, 720–728.

4 A. Ruohola, O. Meurman, S. Nikkari, T. Skottman, A. Salmi, M. Waris, R. Österback, E. Eerola, T. Allander, H. Niesters, T. Heikkinen and O. Ruuskanen, *Clin. Infect. Dis.*, 2006, **43**, 1417–1422.

5 C. D. Bluestone, J. S. Stephenson and L. M. Martin, *Pediatr. Infect. Dis. J.*, 1992, **11**, S7—11.

6 A. G. M. Schilder, T. Chonmaitree, A. W. Cripps, R. M. Rosenfeld, M. L. Casselbrant, M. P. Haggard and R. P.

Venekamp, *Nat. Rev. Dis. Prim.*, 2016, **2**, 1–19.
7 E. LEIBOVITZ, R. SATRAN, L. PIGLANSKY, S. RAIZ, J. PRESS, A. LEIBERMAN and R. DAGAN, *Pediatr. Infect. Dis. J.*, 2003, **22**, 509–514.
8 W. Hong, R. A. Juneau, B. Pang and W. E. Swords, *J. Innate Immun.*, 2009, **1**, 215–224.
9 S. I. Pelton, *Pediatr. Infect. Dis. J.*, 2007, **26**, S1–S25.
10 L. L. Greiner, H. Watanabe, N. J. Phillips, J. Shao, A. Morgan, A. Zaleski, B. W. Gibson and M. A. Apicella, *Infect. Immun.*, 2004, **72**, 4249–4260.
11 W. Hong, B. Pang, S. West-Barnette and W. E. Swords, *J. Bacteriol.*, 2007, **189**, 8300–8307.
12 W. E. Swords, M. L. Moore, L. Godzicki, G. Bukofzer, M. J. Mitten and J. VonCannon, *Infect. Immun.*, 2004, **72**, 106–113.
13 R. Ruhal and R. Kataria, *Microbiol. Res.*, 2021, **251**, 126829.
14 J. A. Jurcisek, J. E. Bookwalter, B. D. Baker, S. Fernandez, L. A. Novotny, R. S. Munson and L. O. Bakaletz, *Mol. Microbiol.*, 2007, **65**, 1288–1299.
15 J. P. Li, C. Z. Hua, L. Y. Sun, H. J. Wang, Z. M. Chen and S. Q. Shang, *J. Pediatr. Adolesc. Gynecol.*, 2017, **30**, 626–631.
16 J. A. Jurcisek and L. O. Bakaletz, *J. Bacteriol.*, 2007, **189**, 3868–3875.
17 L. Ji, A. Buffington and B. Jeske, *Evidence-Based Pract.*, 2019, **22**, 10–11.
18 M. Kiedrowska, A. Kuch, D. Żabicka, I. Waśko, P. Ronkiewicz, K. Wasiak, K. Bojarska, W. Hryniewicz and A. Skoczyńska, *J. Glob. Antimicrob. Resist.*, 2017, **11**, 161–166.
19 S. Maddi, U. Kolsum, S. Jackson, R. Barraclough, B. Maschera, K. D. Simpson, T. G. Pascal, S. Durviaux, E. M. Hessel and D. Singh, *Int. J. COPD*, 2017, **12**, 1507–1518.
20 N. V. S. Vallabani, A. Vinu, S. Singh and A. Karakoti, *J. Colloid Interface Sci.*, 2020, **567**, 154–164.
21 R. S. Hamida, M. A. Ali, D. A. Goda, M. I. Khalil and M. I. Al-Zaban, *Front. Bioeng. Biotechnol.*, 2020, **8**, 1–14.
22 X. Ma, J. Lang, P. Chen and R. Yang, *AIChE J.*, 2021, 1–14.
23 J. Lang, X. Ma, P. Chen, M. D. Serota, N. M. Andre, G. R. Whittaker and R. Yang, *Nanoscale*, 2022, **14**, 3731–3737.
24 A. Khlyustova, M. Kirsch, X. Ma, Y. Cheng and R. Yang, *J. Mater. Chem. B*, 2022, **10**, 2728–2739.
25 P. Chen, J. Lang, Y. Zhou, A. Khlyustova, Z. Zhang, X. Ma, S. Liu, Y. Cheng and R. Yang, *Sci. Adv.*, 2022, **8**, 1–12.
26 J. Wu, X. Wang, Q. Wang, Z. Lou, S. Li, Y. Zhu, L. Qin and H. Wei, *Chem. Soc. Rev.*, 2019, **48**, 1004–1076.
27 M. Comotti, C. Della Pina, R. Matarrese and M. Rossi, *Angew. Chemie - Int. Ed.*, 2004, **43**, 5812–5815.
28 Y. Song, K. Qu, C. Zhao, J. Ren and X. Qu, *Adv. Mater.*, 2010, **22**, 2206–2210.
29 J. Lang, X. Ma, S. S. Liu, D. Streever, M. Serota, T. Donadt, E. R. Loew and R. Yang, *Nanotoday*, 2022, under review.
30 F. Natalio, R. André, A. F. Hartog, B. Stoll, K. P. Jochum, R. Wever and W. Tremel, *Nat. Nanotechnol.*, 2012, **7**, 530–535.
31 W. A. Rutala and D. J. Weber, *Clin. Microbiol. Rev.*, 1997, **10**, 597–610.
32 R. Wever, M. G. M. Tromp, B. E. Krenn, A. Marjani and M. Van Tol, *Environ. Sci. Technol.*, 1991, **25**, 446–449.
33 J. P. Lisher, H. T. Tsui, S. Ramos-Montanez, K. L. Hentchel, J. E. Martin, J. C. Trinidad, M. E. Winkler and D. P. Giedroc, *Msph. Am soc Micro*, 2017, **2**, 1–25.
34 W. Luo, C. Zhu, S. Su, D. Li, Y. He, Q. Huang and C. Fan, *ACS Nano*, 2010, **4**, 7451–7458.
35 K. Herget, H. Frerichs, F. Pfitzner, M. N. Tahir and W. Tremel, *Adv. Mater.*, 2018, **30**, 1–28.
36 R. André, F. Natálio, M. Humanes, J. Leppin, K. Heinze, R. Wever, H. C. Schröder, W. E. G. Müller and W. Tremel, *Adv. Funct. Mater.*, 2011, **21**, 501–509.
37 E. de Boer and R. Wever, *J. Biol. Chem.*, 1988, **263**, 12326–12332.
38 K. Qu, P. Shi, J. Ren and X. Qu, *Chem. - A Eur. J.*, 2014, **20**, 7501–7506.
39 X. He, L. Tan, D. Chen, X. Wu, X. Ren, Y. Zhang, X. He and F. Tang, *Chem. Commun.*, 2013, **49**, 4643–4645.
40 D. Goodacre, M. Blum, C. Buechner, H. Hoek, S. M. Gericke, V. Jovic, J. B. Franklin, S. Kittiwatanakul, T. Söhnel, H. Bluhm and K. E. Smith, *J. Chem. Phys.*, , DOI:10.1063/1.5138959.
41 R. J. G. Nuguid, D. Ferri, A. Marberger, M. Nachtegaal and O. Kröcher, *ACS Catal.*, 2019, **9**, 6814–6820.
42 S. Guan, A. Mori, M. Kato and X. Zhao, *J. Mater. Sci. Mater. Electron.*, 2020, **31**, 9982–9988.
43 M. A. Haija, S. Guimond, A. Uhl, H. Kuhlenbeck and H. J. Freund, *Surf. Sci.*, 2006, **600**, 1040–1047.
44 A. P. and A. M. V. M. P. Casaletto, A. Longo, A. Martorana, *Surf. Interface Anal.*, 2006, **38**, 215–218.
45 J. S. Kumar and P. Thangadurai, *AIP Conf. Proc.*, 2016, **1731**, 2–5.
46 M. L. T. Ronquillo, P. S. Jacinto, P. Ovalle, L. R. Vázquez, E. C. Martínez, E. Marinero and V. Garibay, *Mater. Sci. Appl.*, 2016, **07**, 484–495.
47 M. M. H. Khalil, E. H. Ismail and F. El-Magdoub, *Arab. J. Chem.*, 2012, **5**, 431–437.
48 S. Rajeshkumar, S. V. Kumar, C. Malarkodi, M. Vanaja, K. Paulkumar and G. Annadurai, *Mech. Mater. Sci. Eng.*, 2017, 1–6.
49 J. Khan, S. M. Tarar, I. Gul, U. Nawaz and M. Arshad, *3 Biotech*, 2021, **11**, 1–15.
50 P. S. Stewart, *Int. J. Med. Microbiol.*, 2002, **292**, 107–113.
51 R. Yang, V. Sabharwal, N. Shlykova, O. S. Okonkwo, S. I. Pelton and D. S. Kohane, *JCI insight*, , DOI:10.1172/jci.insight.123415.
52 R. Yang, V. Sabharwal, N. Shlykova, O. S. Okonkwo, S. I. Pelton and D. S. Kohane, *JCI insight*, 2018, **3**, 1–10.
53 V. Sabharwal, M. Figueira, S. I. Pelton and M. M. Pettigrew, *Microbes Infect.*, 2012, **14**, 712–718.
54 Q. Liu, A. Zhang, R. Wang, Q. Zhang and D. Cui, *A Review on Metal- and Metal Oxide-Based Nanozymes: Properties, Mechanisms, and Applications*, Springer Singapore, 2021,

vol. 13.

55 T. Dvir, B. P. Timko, D. S. Kohane and R. Langer, *Nat. Nanotechnol.*, 2011, **6**, 13–22.

56 H. Liu, B. Haider, H. R. Fried, J. Ju, O. Bolonduro, V. Raghuram and B. P. Timko, *Nano Res.*, 2018, **11**, 5372–5399.

57 F. Patolsky, B. P. Timko, G. Yu, Y. Fang, A. B. Greytak, G. Zheng, C. M. Lieber, E. Kim and E. Kim, .

58 D. P. Erdosy, M. B. Wenny, J. Cho, C. DelRe, M. V. Walter, F. Jiménez-Ángeles, B. Qiao, R. Sanchez, Y. Peng, B. D. Polizzotti, M. O. de la Cruz and J. A. Mason, *Nature*, 2022, **608**, 712–718.